Available online at www.sciencedirect.com
ScienceDirect
Journal of Power Sources 176 (2008) 428–434
JOURNAL OF POWER SOURCES
www.elsevier.com/locate/jpowsour

Properties of high-temperature PEFC Celtec®-P 1000 MEAs in start/stop operation mode

Thomas J. Schmidt *, Jochen Baurmeister

BASF Fuel Cell GmbH, Industrial Park Hoechst, G865, D-65926 Frankfurt, Germany

Available online 28 August 2007

Abstract

This paper aims at the comparison of two differently operated Celtec®-P 1000 MEAs: one MEA is operated in a start/stop cycling mode (12 h operation at 160 °C followed by 12 h shutdown), the other MEA is continuously operated at 160 °C. We demonstrate more than 6000 h total operation time with more than 240 start/stop cycles, while the test is still ongoing. The degradation rate is 0.2 mV cycle^{-1} or 11 μV h^{-1} on a time basis. The continuously operated MEA is operated more than 6000 h with a degradation rate of approximately 5 μV h^{-1}. Through separation of the individual cathodic loss terms, a detailed insight into the doubled time-based degradation rate under start/stop cycling conditions could be given. Both Ohmic resistances and oxygen reduction overpotentials are basically identical in MEAs under continuous and start/stop cycling operation. In the start/stop cycled MEA, however, significantly increased cathodic mass transport overpotentials are observed as a result of enhanced corrosion of the cathode catalyst support, which confirms the generally discussed reverse-current mechanism under start/stop cycling conditions. Results from a newly developed MEA demonstrate that this mechanism can successfully be mitigated through improvement of the materials used in the MEA.

Keywords: Polybenzimidazole (PBI); High-temperature PEFC; Start–stop durability

1. Introduction

BASF Fuel Cell (formerly PEMEAS GmbH) produces polybenzimidazole (PBI)-based high-temperature membrane electrode assemblies (MEAs) commercialized and sold under the brand name Celtec®. These MEAs are operating at temperatures between 120 °C and 180 °C, and, therefore, are especially suitable in reformed-hydrogen-based PE fuel cells. Due to these high operating temperatures, CO tolerances up to 3% can be achieved. Additional fuel gas impurities (inorganic or organic, such as H_2S or methanol) can be tolerated to a much higher concentration than in low-temperature fuel cells based on PFSA-type or hydrocarbon membranes. That is, in a fuel cell system using a fuel processor for reforming hydrocarbon-based fuels, the gas purification can be simplified and, *e.g.*, the use of a preferential oxidation stage in the fuel processing line in order to reduce the CO concentration can be avoided. Additionally, from a system engineering point of view, due to the high stack operating temperatures of up to 180 °C, fuel processors can easily be thermally integrated within the stack. For example, from a stack using PBI-based MEAs, waste heat can be effectively used to provide heat for a methanol steam reformer when both stack and fuel processor are appropriately thermally packaged [1].

Due to the inherent differences in the proton conductivity mechanisms in the Celtec® membranes (Grotthus mechanism) versus PFSA-type membranes (water assisted shuttle mechanism) [2], in high-temperature PE fuel cells, no external humidification of the gases is necessary, which leads to a significant reduction of complexity and cost in high-temperature fuel cell systems. Additional issues due to membrane decomposition from peroxide can be avoided with Celtec® membranes due to the inherent higher stability of PBI versus PFSA membranes and the high operating temperature where the survival time of hydrogen peroxide is minimized.

Finally, from a fuel cell system perspective, waste heat can be effectively used (either co-generation of heat and power, CHP systems, or even tri-generation systems, where waste heat can be also used for cooling purposes). This is increasing the overall systems efficiency drastically versus low-temperature fuel cell systems.

Although several distinct advantages of high-temperature stack operation can be outlined, care has to be taken when

* Corresponding author.
E-mail address: thomas.justus.schmidt@basf.com (T.J. Schmidt).

0378-7753/$ – see front matter © 2007 Elsevier B.V. All rights reserved.
doi:10.1016/j.jpowsour.2007.08.055

selecting the materials for high-temperature MEAs. The catalyst materials must be highly active for the oxidation of realistic reformates and the oxygen reduction reaction, but in addition, high stability towards corrosion is needed in order to ensure long fuel cell lifetimes especially when the stack is operated under realistic conditions. For example, realistic fuel cell operation conditions not only mean operation with real reformates derived from a fuel processor, but also typically involves temperature and start/stop cycling. Especially start/stop cycling exhibit high stress to the cathode due to local excursions to high potentials above 1.3 V, where significant corrosion of the cathode carbon materials occurs. Details on the mechanism of cathodic potential excursions during start/stop phases can be found in Refs. [3,4].

In this contribution, the impact of start/stop cycling of high-temperature Celtec®-P 1000 MEAs on the cathode stability will be demonstrated. In order to gain insights, two durability tests will be demonstrated. One fuel cell test is operated in a 12 h operation/12 h shut down mode, where during the shut down the cell was allowed to cool to 20–25 °C. For comparison, the second fuel cell test is continuously operated without performing any shut down. Although the degradation rate of MEAs under start/top conditions is increased versus continuously operated MEAs, the results still demonstrate exceptionally high MEA stability under the chosen conditions.

2. Degradation mechanisms related to start/stop cycling

During start/stop cycling the two predominant mechanisms which can affect MEA durability is (i) corrosion of the cathode due to potential excursions to $E > 1.3$ V [3,5] and (ii) electrolyte redistribution due to volume expansions/contractions. The latter mode is unique to fuel cell operation with at least partly liquid electrolyte whereas the first is a more general mode observed also in low temperature PEFCs.

Cathode carbon corrosion during start–stop cycling occurs when the cathode electrolyte potential excurses to high values when H_2/air (air/H_2) fronts are passing through the anode and the cathode compartment is filled with air. Locally around the H_2/air (air/H_2) front this potential can be as high as 1.5 V [3] and can be considered as internal short-circuiting of the MEA. Own measurements in a dual cell setup as proposed, *e.g.*, in Ref. [6] at 160 °C resulted in cathodic potentials around 1.4 V versus a reversible hydrogen electrode and currents of up to 800 mA. Quantitative results on these measurements will be published elsewhere [7]. Carbon corrosion currents at operating temperatures of 160 °C or higher can be quite large (*e.g.*, for Vulcan XC 72 at 180 °C and 1.0 V, corrosion currents of 1–10 mA mg_{carbon}^{-1} are observed [8–11]). These currents are high enough to completely oxidize the cathodic carbon in a rather short period of time. The main effect from carbon corrosion is an increase in the hydophilicity of the cathodic catalyst layer concomitant with electrolyte flooding which, in turn, leads to increase of the cathode mass transport overpotentials. Concomitant with the corrosion of the carbon, thinning of the catalyst layer and loss of its void volume is observed. In a worst-case scenario, complete deterioration of the carbon finally would affect the structural integrity of the cathode. It should be noted at this place, that carbon corrosion is a strong function of temperature, potential and water partial pressure [8,10].

Electrolyte redistribution mainly occurs due to temperature- and concentration-induced volume expansions and contractions of the liquid electrolyte. The first is a straightforward effect when liquids undergo temperature cycling. The latter represents a thermodynamic effect pronounced for hygroscopic electrolytes like phosphoric acid, sulfuric acid or alkaline electrolytes, respectively, which always tend to equilibrate with the environment. That is, these liquids change their concentration as a function of temperature and water partial pressures (relative humidities). Low relative humidities and high temperatures lead to highly concentrated solutions, whereas at low temperatures with increasing relative humidities the concentration decreases due to the hygroscopic properties of the electrolytes. It must be noted, however, that electrolyte redistribution appears to be minor under start/stop cycling conditions in PBI-based MEAs since the membrane can compensate for most of the volume changes (in contrast, *e.g.*, to a SiC electrolyte matrix in phosphoric acid fuel cells).

3. Experimental

3.1. Membrane

Celtec®-P membranes are polymer gels containing polybenzimidazole (PBI) and phosphoric acid. Although described elsewhere already in more detail [11–13], a short introduction in the general membrane chemistry will be given here. Polymerization of the monomers, *e.g.*, tetra-amino biphenyl and an aromatic di-carboxylic acid, is done in polyphosphoric acid (PPA), *i.e.*, phosphoric acid with concentrations above 100%, at elevated temperatures producing a sol containing PBI/PPA. From the PBI/PPA sol the membrane is casted and further hydrolyzed. During the hydrolysis, the membrane undergoes a sol–gel transition which results in the final membrane used in Celtec® MEAs. The final membrane has a phosphoric acid content of more than 95 wt% or up to 70 phosphoric acid molecules per PBI repeat unit. Note that this approach is completely different to the approaches described elsewhere, *i.e.*, the production of a PBI film which is subsequently soaked in phosphoric acid [14–17]. This dip-and-soak or imbibing process, depending on the PBI composition, only results in membranes with ca. 5–15 phosphoric acid molecules per PBI repeat unit [16]. A detailed comparison of different PBI-based membranes can be found in a recent review [18].

3.2. Membrane electrode assemblies

Celtec®-P 1000 MEAs are produced at BASF Fuel Cell GmbH (Frankfurt, Germany) using Celtec®-P membranes and electrodes produced at BASF Fuel Cell Inc. (Somerset, NJ, USA). The cathode contains a Vulcan XC 72 supported Pt-alloy with 0.75 $mg_{Pt}\,cm^{-2}$. The anode contains a Vulcan XC 72 supported Pt catalyst with 1 $mg_{Pt}\,cm^{-2}$. Membrane thickness in the MEA is approximately 50–75 μm.

3.3. MEA tests

The tests for demonstrating the impact of start/stop cycling on cathode degradation as well as the continuous operation test are carried out in 50 cm^2 single cell setups using graphite flow field plates. Unless otherwise noted, the cells are operated at 160 °C and ambient pressure using dry fuel and air with stoichiometries of 1.2 and 2, respectively. In the course of the tests, several sets of H_2–air ($\lambda_{air} = 2$) and H_2–O_2 ($\lambda_{O_2} = 9.5$) polarization curves are recorded in order to gain insight into the different cathode degradation modes. Ohmic cell resistances are measured with 1 kHz ac impedance measurements.

The start/stop cycling test of the MEA is performed in a way, that the cell was continuously operated for 12 h at 0.2 A cm^{-2} before cell operation is stopped and the cell is allowed to cool down to 20–25 °C. Note that the cell was not actively purged with any gas during the stop period. After the 12 h stop period, the cell is again restarted, *i.e.*, one shut down per day is performed. During the stop phase, no reactant gases are flowing. The gas outlets of the cell are kept open throughout the whole experiment directly at the cell end plates. That is under all conditions, approximately 2 cm from the cell outlets in upstream direction the flow fields begin. That way, a short diffusion path is given which allows easy equilibrium of the gases in the cell with the environmental air and it is ensured that air can penetrate the anode compartment. For comparison purposes another cell is operated continuously at 0.2 A cm^{-2} without performing any start/stop cycles.

3.4. Tafel slope analysis

In order to gain insight into the different cathode degradation modes, the recorded polarization curves are analyzed doing a Tafel analysis at the beginning of life and through the course of the test. The initial IR-free cell performances using H_2–air and H_2–O_2 are shown in Fig. 1 along with the equilibrium potential at each operating point for pure oxygen operation. Note that the decrease of the equilibrium potential at small current densities is a result of increasing water partial pressure when the gases are supplied in a constant minimum flow before the stoichiometric gas flow begins at 60 mA cm^{-2}. A single Tafel slope of approximately 90 mV dec^{-1} can be fitted throughout the whole current density range (white squares in Fig. 1). The fitted slope of 90 mV dec^{-1} closely reflects the theoretical value of $2.303RT/F$ (86 mV dec^{-1} at 160 °C) and directly points to pure kinetic reaction control without interference of mass transport losses. The same Tafel slope can be fitted for the H_2–air polarization curve (grey squares in Fig. 1), although only up to 0.1 A cm^{-2}. At higher current densities, the plot significantly deviates from linearity pointing to the presence of the well-known mass transport resistances when using air as the oxidant. Following an analysis described in detail in Refs. [11,19,20], the IR-free cell potential, $E_{cell,IR\text{-}free}$, can be given by the following equation:

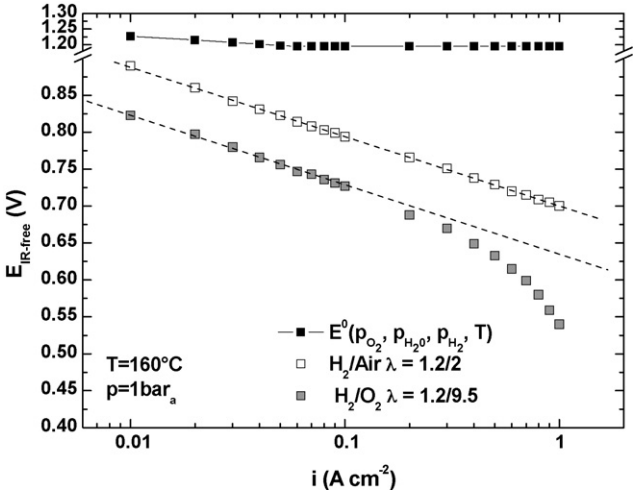

Fig. 1. Beginning of life Tafel plot of a typical Celtec®-P 1000 MEA when operated with H_2–air (stoich 1.2/2, grey squares) and H_2–O_2 (stoich 1.2/9.5, white squares). $T = 160$ °C, $p = 1$ bar_a. The equilibrium potential (black squares) at each operating point is illustrated for reference.

$$E_{cell,IR\text{-}free} = E^0(p_{H_2/O_2/H_2O}, T) - \eta_{ORR} - \eta_{cathode,mtx} - \eta_{HOR} - \eta_{anode,mtx} \quad (1a)$$

where $E^0(p_x,T)$ represents the temperature and H_2, O_2, and H_2O partial pressure dependent equilibrium potential, η_{ORR} and η_{HOR} the kinetic overpotentials for the oxygen reduction and hydrogen oxidation reaction and $\eta_{x,mtx}$ is the mass transport overpotentials on the cathode and anode, respectively. The temperature and partial pressures dependent equilibrium potential $E^0(p_x,T)$ is calculated according to the following equation:

$$E^0(p_{H_2/O_2/H_2O}, T) = E^{0,*} + \frac{\partial E^{0,*}}{\partial T}(T - 298\,K) + \left(\frac{2.303RT}{2F}\right)\log\left(\frac{\bar{p}_{H_2}\bar{p}_{O_2}^{0.5}}{\bar{p}_{H_2O}}\right) \quad (1b)$$

where the first term, $E^{0,*}$, is the equilibrium potential at 298 K and 101,325 Pa calculated from ΔG values for gas phase water [21]; the second term is used to correct $E^{0,*}$ for the temperature, calculated using ΔS values for gas phase water [21]; the third Nernstian term corrects $E^{0,*}$ for the individual partial pressures. $\bar{p}_{H_2}$, $\bar{p}_{O_2}$, $\bar{p}_{H_2O}$ are the mean partial pressures under operation conditions of hydrogen, oxygen and water, respectively, normalized to 101,325 Pa.

All anodic overpotentials are negligible under the applied conditions which was checked by polarization measurements with increased and decreased hydrogen utilizations. Additionally, as concluded from Fig. 1, the oxygen polarization curve is under pure kinetic reaction control and no mass transport resistances are present. That is Eq. (1a) reduces to

$$E_{cell,IR\text{-}free} = E^0(p_{H_2/O_2/H_2O}, T) - \eta_{ORR} \quad (1c)$$

By proper calculation of $E^0(p_x,T)$, the oxygen reduction overpotential can be determined by Eq. (1c) from the measured oxygen polarization curve which follows a oxygen partial pressure dependent Butler–Volmer expression [20,22]. The theoretical Tafel line for air polarization should be just shifted to lower cell

potentials, see Fig. 1, by ΔE_{O_2-air} given by

$$\Delta E_{O_2-air} = \Delta E^0 + b\gamma \log\left(\frac{p_{O_2}}{p_{air}}\right) \quad (2)$$

with ΔE^0 being the difference between the equilibrium potentials for pure oxygen and air, b and γ are the Tafel slope ($b = 2.3RT/F$) and the kinetic reaction order ($\gamma \approx 0.6$; defined as the logarithmic change of the current density with the oxygen partial pressure at constant temperature and overpotential [23]) and p_x being the partial pressures for pure oxygen and air. Deviations from the theoretical Tafel line for air polarization to lower cell potentials can be considered to be cathodic mass transport overpotentials.

4. Results and discussion

In order to study the start/stop behavior of a Celtec®-P 1000 MEA, we operate a single cell in start/stop cycling mode (12 h operation followed by 12 h shut down with cooling to room temperature). Fig. 2 illustrates the cell potential at 0.2 A cm^{-2} as a function of the number of start/stop cycles. Currently, this test is operated for more than 6000 h including more than 240 start/stop cycles where the cell is cooled down to room temperature. A cycle-number-based degradation rate of 0.2 mV per cycle (based on 240 cycles) can be calculated for these operating conditions. For better comparison to MEAs operated continuously, Fig. 3 shows the lifetime based cell potential of the cycled MEA, blue squares, and a MEA operated continuously at 0.2 A cm^{-2}, red circles. Both cells exhibit the typical logarithmic-type time-based degradation behavior often observed in fuel cells (see, *e.g.*, [24–27]). Despite this logarithmic behavior, for simplicity, we will express the degradation as if it would be a linear relationship, which is valid in this case since both cells are operated for a very similar timeframe. For the continuously operated fuel cell, a degradation rate of 5 μV h^{-1} (based on 6300 h) is observed whereas for the cell with the 240 start/stop cycles, the time-based degradation rate is calculated to be 11 μV h^{-1} (based on 6100 h). Quite obviously, due to the start–stop cycling, the

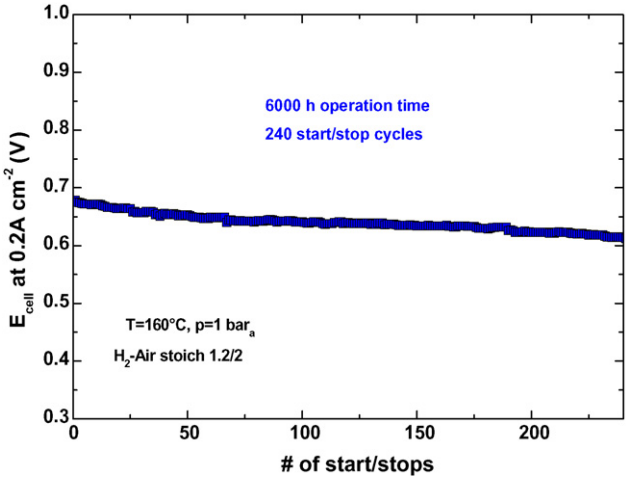

Fig. 2. Cell potentials at 0.2 A cm^{-2} as a function of start/stop cycles. H_2–air (stoich 1.2/2), $T = 160\,^{\circ}C$, $p = 1\,bar_a$.

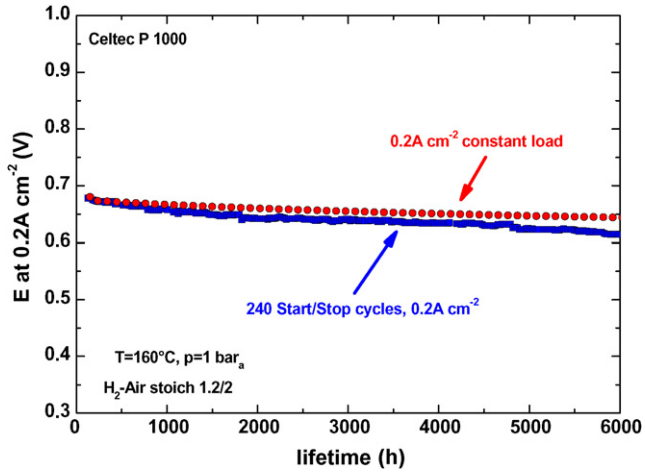

Fig. 3. Cell potentials at 0.2 A cm^{-2} as a function of lifetime of a constant load test without start/stop cycling (red circles) and of the start/stop cycle test (blue squares). H_2–air (stoich 1.2/2), $T = 160\,^{\circ}C$, $p = 1\,bar_a$. (For interpretation of the references to color in this figure legend, the reader is referred to the web version of the article.)

degradation rate is doubled when the cell is start/stop cycled. In other words, the absolute voltage loss over the same period of time is roughly doubled for the start/stop cycled cell. In what follows, we will analyze the origin of the voltage losses for both cells using the aforementioned Tafel slope analysis.

4.1. Ohmic cell resistance

The Ohmic cell resistance as a function of lifetime for both cells under investigation is illustrated in Fig. 4. Generally, in both cells, independent of operation mode, the Ohmic cell resistance is increasing slightly from 70 mΩ cm^2 to 90 mΩ cm^2 within the course of the test with quasi-identical functionality. This identical behavior demonstrates that start/stop cycling does not

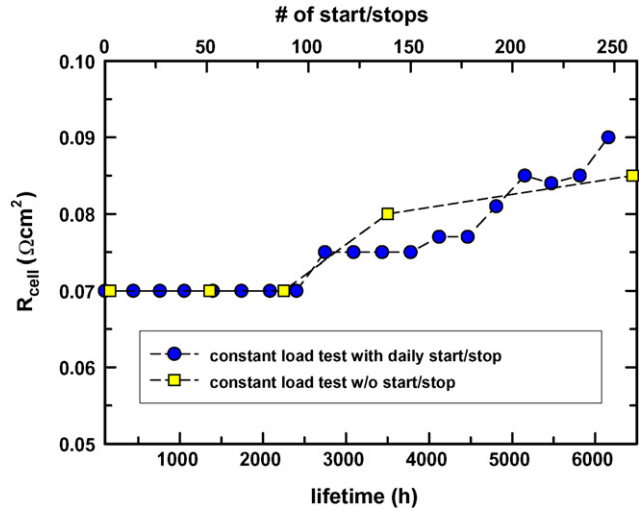

Fig. 4. Ohmic cell resistance measured by 1 kHz ac impedance measurements at 0.2 A cm^{-2} of the continuously operated cell (red circles) and the start/stop cycled cell (blue squares). (For interpretation of the references to color in this figure legend, the reader is referred to the web version of the article.)

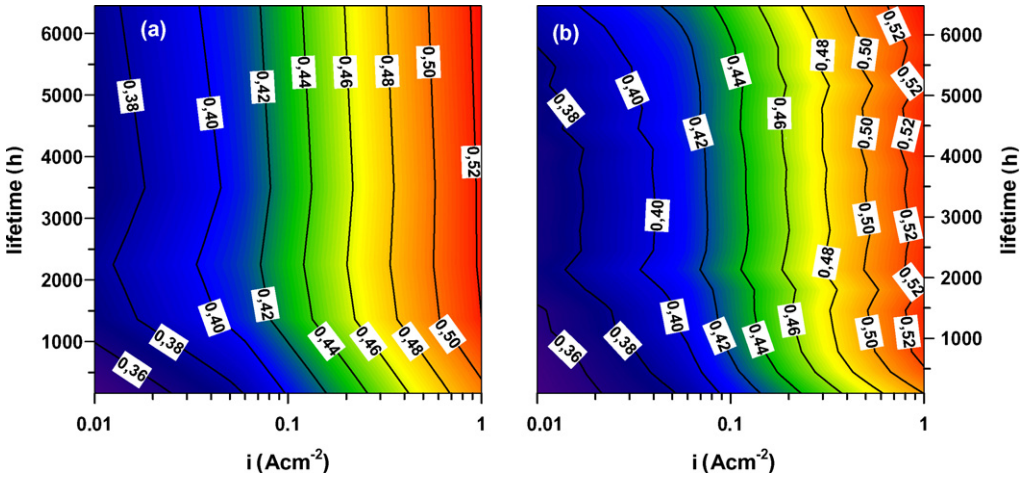

Fig. 5. Oxygen reduction overpotentials as a function of lifetime and current densities for (a) constant operation test and (b) start/stop cycling test calculated according to Eq. (1a) from H_2–O_2 polarization curves.

adversely affect the IR-drop and therefore, is not responsible for the observed differences in overall degradation rate.

4.2. Oxygen reduction kinetics

In order to get insight into the oxygen reduction kinetics, H_2–O_2 polarization curves were recorded at the beginning of life and throughout the course of the tests. After correction for the IR-drop, the oxygen overpotentials are calculated using Eq. (1c) and plotted as functions of current density and operation time in Fig. 5. The oxygen polarization curves can be fitted with straight lines, Fig. 1, with consistent Tafel slopes between 90 mV dec^{-1} and 94 mV dec^{-1}. The Tafel slope fits were linear over the complete current density range, and only after longer operation times (>4000 h), deviations from linearity to lower cell voltages was observed and the fits were only executed up to 0.2 A cm^{-2}. The values of the Tafel slope, which basically represent the theoretical value (2.3*RT*/*F*), indicate that the cathode is only kinetically limited. The deviations from linearity at longer operation times, however, points to the presence of mass transport resistances which we will discuss in the next section in more detail. A closer comparison of the oxygen reduction overpotentials (Fig. 6) of the continuously operated and start/stop cycled MEA, respectively, shows very similar behavior with respect to operation time and current density. For better comparison, the increase of overpotential, ΔE_{ORR}, is calculated with the following equation:

$$\Delta E_{ORR} = \eta_{ORR,BOL} - \eta_{ORR,t} \quad (3)$$

with $\eta_{ORR,t}$ and $\eta_{ORR,BOL}$ being the overpotential at given operation time and at beginning of life, respectively. As an example, this difference in overpotential at 0.2 A cm^{-2} is plotted in Fig. 7. Quite obviously, both MEAs exhibit very similar logarithmic behavior with an initial fast increase in overpotential in the first 1000 h operation followed by rather stable values for longer operation times. Based on a Tafel slope of approximately 90 mV dec^{-1}, an increase in oxygen overpotentials by ca. 30 mV, Fig. 6, can be translated to a reduction of the electrochemical active surface area by approximately 50%. This value was confirmed by 53% reduction of the H_{upd} charges in cyclic voltammetry measurements at the beginning versus end of life of the continuously operated MEA (note, the start/stop cycled MEA is still ongoing and no end of life analysis is performed yet). The reduction can be mainly related to catalyst particle growth during operation in the first 500–1000 h. In order to give an impression, reduction of the Pt surface area by 50% is obtained, when catalyst nanoparticles grow from an initial mean diameter of 3 nm to a mean particle diameter of 6 nm [28], which represents a rather realistic scenario in fuel cell cathodes [29].

As a conclusion from this section, oxygen reduction overpotentials are increasing rather identically for both MEAs under investigation, *i.e.*, start/stop cycling does not adversely affect the cathode catalyst kinetics.

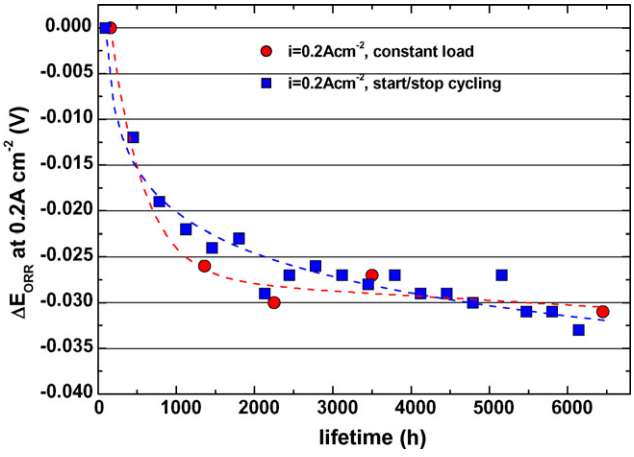

Fig. 6. Changes in oxygen reduction overpotentials vs. lifetime for MEA in constant operation (red circles) and start/stop cycling mode (blue squares), respectively. Data are derived from Fig. 5. (For interpretation of the references to color in this figure legend, the reader is referred to the web version of the article.)

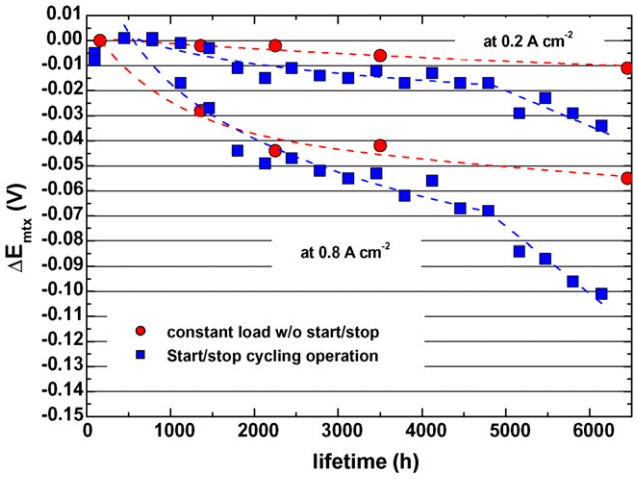

Fig. 7. Changes in mass transport overpotentials in H_2–air operation vs. lifetime for MEA in constant operation (red circles) and start/stop cycling mode (blue squares) at 0.2 A cm^{-2} and 0.8 A cm^{-2}, respectively. (For interpretation of the references to color in this figure legend, the reader is referred to the web version of the article.)

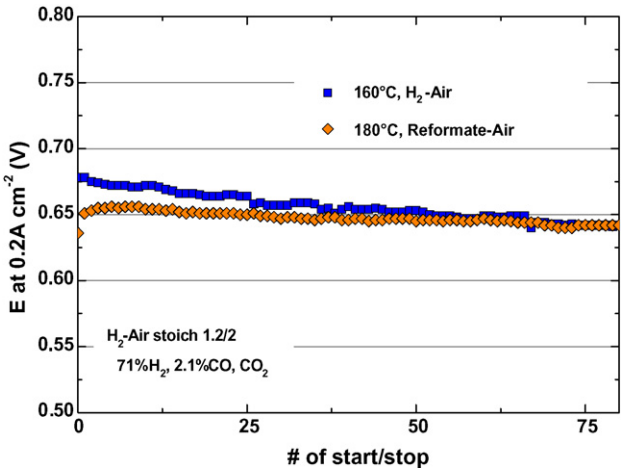

Fig. 8. Cell potentials at 0.2 A cm^{-2} as a function of start/stop cycles for H_2–air (stoich 1.2/2), $T = 160\,^{\circ}C$, $p = 1\,bar_a$ (blue squares) and for a developmental MEA operated at 180 °C using reformate ($\lambda_{H_2} = 1.45$) with 71% H_2, 2.1% CO and balance CO_2. (For interpretation of the references to color in this figure legend, the reader is referred to the web version of the article.)

4.3. Mass transport overpotentials

Finally, after demonstrating that neither differences in Ohmic resistances nor in the cathode kinetics are observed for both cells, we analyze the cathodic mass transport behavior of the MEAs as described above using Eq. (1a)–(1c) and (2). Similar than performed for Fig. 6, the increase of mass transport overpotential, ΔE_{mtx}, is calculated with the following equation:

$$\Delta E_{mtx} = \eta_{mtx,BOL} - \eta_{mtx,t} \quad (4)$$

with $\eta_{mtx,t}$ and $\eta_{mtx,BOL}$ being the mass transport overpotential when operated with air at given operation time and at beginning of life, respectively. The result is plotted in Fig. 7 for both the constant operation and start/stop cycled MEA at 0.2 A cm^{-2} and 0.8 A cm^{-2}, respectively. As expected from the underlying carbon corrosion process, the mass transport properties of the start/stop cycled MEA significantly differs from the mass transport properties of the continuously operated cell. Interestingly, at short operation times below 1000 h operation, in the start/stop cycled cell, the mass transport slightly improves, which may be interpreted with some beneficial redistribution of the electrolyte within the MEA. After this initial improvement, however, mass transport overpotentials increase significantly. After 5000 h operation, *e.g.*, mass transport overpotentials for the cycled cell at 0.8 A cm^{-2} are roughly 30 mV higher compared to the continuously operated MEA. This behavior can be related to increased carbon corrosion of the cathode catalyst support [11] during start/stop cycling as described in a previous section. As a result, the cathode becomes more and more hydrophilic and, as a consequence, increasingly flooded with phosphoric acid which leads to increased mass transport resistances [30–32]. One should keep in mind, however, that carbon corrosion, especially in a later stage of the tests performed here, also may change the porous structure of the cathode catalyst layer concomitant with a void volume loss [33,34]. This in turn means that the electrolyte will be distributed in an unfavorable way leading to increase in mass transport overpotentials. One can conclude, hence, that the main degradation mechanism during start/stop cycling of Celtec® MEAs is electrolyte flooding of the cathode due to corrosion of the cathode catalyst support.

4.4. Outlook

After identifying the main degradation mode during start/stop cycling, there are some mitigation strategies which can be implemented in order to increase the stability of MEAs operated under conditions where corrosion issues are predominant. One feasible way is external potential control of the MEA [35,36]. This system solution simply avoids potential excursions of the cathode during start/stop cycling, and therefore carbon corrosion issues are suppressed. Besides system solutions (for a useful summary, see Ref. [4]), also the intrinsic stability of the materials used in the MEA with respect to corrosion can be improved. Therefore, in Fig. 8, we finally compare the first 75 start/stop cycles of the Celtec®-P 1000 MEA taken from Fig. 2 with the behavior of a developmental MEA operated under even more severe operating temperatures of 180 °C (with reformate containing 2.1%CO instead of pure hydrogen, see figure caption). Note that only the higher operating temperature typically increases degradation of the cathode. Quite obviously, despite the higher operating temperature, the degradation of the developmental MEA is lower by a factor of 7 versus Celtec®-P 1000 due to improvement of the corrosion stability of the materials used in the MEA. This development, finally, will be implemented into a new generation of high-temperature PEFC Celtec® MEA.

5. Summary

In this publication, two differently operated Celtec®-P 1000 MEAs are compared. One MEA is operated in a start/stop cycling mode (12 h operation at 160 °C followed by 12 h shutdown), the other MEA is continuously operated at 160 °C. The

start/stop cycling MEA is operated for a total of more than 6000 h including more than 240 start/stop cycles. The degradation rate is 0.2 mV cycle^{-1} or 11 μV h^{-1} on a time basis. The continuously operated MEA is operated more than 6000 h with a degradation rate of approximately 5 μV h^{-1}. Through separation of the individual cathodic loss terms using a Tafel slope analysis, a detailed insight into the doubled time-based degradation rate under start/stop cycling conditions could be given. We showed that both Ohmic resistances and oxygen reduction overpotentials are basically identical in MEAs under continuous and start/stop cycling operation. In the start/stop cycled MEA, however, significantly increased cathodic mass transport overpotentials are observed as a result of enhanced corrosion of the cathode catalyst support, which confirms the generally discussed reverse-current mechanism under start/stop cycling conditions. Results from a newly developed MEA demonstrate that this mechanism can successfully be mitigated through improvement of the materials used in the MEA.

References

[1] J.N. Allen, N. Sifer, E. Bostic, Proceedings of the 42nd Power Sources Conference, Philadelphia, 2006, p. 403.
[2] K.D. Kreuer, S.J. Paddison, E. Spohr, M. Schuster, Chem. Rev. 104 (2004) 4678.
[3] C.A. Reiser, L.J. Bregoli, T.W. Patterson, J.S. Yi, J.D. Yang, M.L. Perry, T.D. Jarvi, Electrochem. Sol. Lett. 8 (2005) A273.
[4] M.L. Perry, T.W. Patterson, C.A. Reiser, ECS Trans. 3 (2006) 783.
[5] R. Makharia, S.S. Kocha, P.T. Yu, M.A. Sweikart, W. Gu, F.T. Wagner, H.A. Gasteiger, ECS Trans. 1 (2006) 3.
[6] H. Tang, Z. Qi, M. Ramani, J.F. Elter, J. Power Sources 158 (2006) 1306.
[7] T.J. Schmidt, in press.
[8] P. Stonehart, Carbon 22 (1984) 423.
[9] K. Kinoshita, Electrochemical and Physicochemical Properties, vol. 44, John Wiley & Sons, New York, 1988.
[10] P.L. Antonucci, F. Romeo, M. Minutoli, E. Alderucci, N. Giordano, Carbon 26 (1988) 197.
[11] T.J. Schmidt, ECS Trans. 1 (2006) 19.
[12] L. Xiao, H. Zhang, E. Scanlon, L.S. Ramanathan, E.-W. Choe, D. Rogers, T. Apple, B. Benicewicz, Chem. Mater. 17 (2005) 5328.
[13] L. Xiao, H. Zhang, E. Scanlon, R. Chen, E.-W. Choe, L.S. Ramanathan, S. Yu, B. Benicewicz, Fuel Cells 5 (2005) 287.
[14] R. Savinell, E. Yeager, D. Tryk, U. Landau, J. Wainright, D. Weng, K. Lux, M. Litt, C. Rogers, J. Electrochem. Soc. 141 (1994) L46.
[15] J.-T. Wang, R.F. Savinell, J. Wainright, M. Litt, H. Yu, Electrochim. Acta 41 (1996) 193.
[16] J.S. Wainright, M.H. Litt, R.F. Savinell, in: W. Vielstich, A. Lamm, H.A. Gasteiger (Eds.), Handbook of Fuel Cells. Fundamentals, Technology and Applications, vol. 3, John Wiley & Sons, New York, 2003, p. 436.
[17] Q. Li, R. He, J.O. Jensen, N.J. Bjerrum, Fuel Cells 4 (2004) 147.
[18] J. Mader, L. Xiao, T.J. Schmidt, B. Benicewicz, in: G.G. Scherer (Ed.), Adv. Polym. Sci., Springer, in press.
[19] H.A. Gasteiger, W. Gu, M. Makharia, M.F. Mathias, B. Sompalli, in: W. Vielstich, H.A. Gasteiger, A. Lamm (Eds.), Handbook of Fuel Cells—Fundamentals, Technology and Applications, vol. 3: Fuel Cell Technology and Applications, Part 1, 1st ed., John Wiley & Sons, Chichester, 2003, p. 593.
[20] K.C. Neyerlin, H.A. Gasteiger, C.K. Mittelstaedt, J. Jorne, W. Gun, J. Electrochem. Soc. 152 (2005) A1073.
[21] D.R. Lide, CRC Handbook of Chemistry and Physics, CRC Press, Boca Raton, FL, 1995.
[22] J.S. Newman, Electrochemical Systems, Prentice Hall, Englewood Cliffs, NJ, 1973.
[23] K.C. Neyerlin, W. Gu, J. Jorne, H.A. Gasteiger, J. Electrochem. Soc. 153 (2006) A1955.
[24] D.N. Patel, H.C. Maru, M. Farooque, C.H. Ware, J. Electrochem. Soc. 131 (1984) 2750.
[25] K. Strasser, in: W. Vielstich, A. Lamm, H.A. Gasteiger (Eds.), Handbook of Fuel Cells. Fundamentals, Technology and Applications, 1st ed., John Wiley & Sons, New York, 2003, p. 1201.
[26] D.P. Wilkinson, J. St.-Pierre, in: W. Vielstich, H.A. Gasteiger, A. Lamm (Eds.), Handbook of Fuel Cells—Fundamentals, Technology and Applications, vol. 3: Fuel Cell Technology and Applications, Part 1, 1st ed., John Wiley & Sons, Chichester, 2003, p. 611.
[27] R.-H. Song, D.R. Shin, C.S. Kim, S.-H. Soi, J. New. Mater. Electrochem. Sys. 2 (1999) 131.
[28] P. Stonehart, J. Appl. Electrochem. 22 (1992) 995.
[29] T. Tada, in: W. Vielstich, H.A. Gasteiger, A. Lamm (Eds.), Handbook of Fuel Cells—Fundamentals, Technology and Applications, vol. 3: Fuel Cell Technology and Applications, Part 1, 1st ed., John Wiley & Sons, Chichester, 2003, p. 481.
[30] H.R. Kunz, G.A. Gruver, J. Electrochem. Soc. 122 (1975) 1279.
[31] K. Kinoshita, Electrochemical Oxygen Technology, John Wiley & Sons, New York, 1992.
[32] M.L. Perry, J. Newman, E.J. Cairns, J. Electrochem. Soc. 145 (1998) 5.
[33] T.W. Patterson, R.M. Darling, Electrochem. Sol. Let. 9 (2006) A183.
[34] P.T. Yu, W. Gu, M. Makharia, F.T. Wagner, H.A. Gasteiger, ECS Trans. 3 (2006) 797.
[35] D.A. Condit, R.D. Breault, US 6,635,370 (2003).
[36] T.A. Bekkedahl, L.J. Bregoli, R.D. Breault, E.A. Dykeman, J.P. Meyers, T.W. Patterson, T. Skiba, C. Vargas, D. Yang, J.S. Yi, US 6,913,845 (2005).